

# Mapping the Inhomogeneous Electrochemical Reaction Through Porous $\text{LiFePO}_4$ -Electrodes in a Standard Coin Cell Battery

Fiona C. Strobridge,<sup>†,○</sup> Bernardo Orvananos,<sup>‡,○</sup> Mark Croft,<sup>§,||</sup> Hui-Chia Yu,<sup>‡</sup> Rosa Robert,<sup>†,#</sup> Hao Liu,<sup>†</sup> Zhong Zhong,<sup>||</sup> Thomas Connolly,<sup>⊥</sup> Michael Drakopoulos,<sup>⊥</sup> Katsuyo Thornton,<sup>‡</sup> and Clare P. Grey<sup>\*,†,⊗</sup>

<sup>†</sup>Department of Chemistry, University of Cambridge, Lensfield Road, Cambridge, Cambridgeshire CB2 1EW, U.K.

<sup>‡</sup>Department of Materials Science and Engineering, University of Michigan, Ann Arbor, Michigan 48109, United States

<sup>§</sup>Department of Physics and Astronomy, Rutgers University, Piscataway, New Jersey 08854, United States

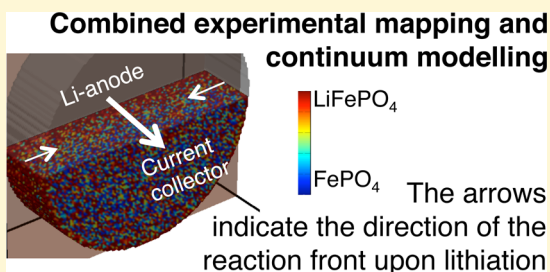
<sup>||</sup>National Synchrotron Light Source, Brookhaven National Laboratory, Upton, New York 11973, United States

<sup>⊥</sup>Diamond Light Source Limited, Harwell Science and Innovation Campus, Didcot, Oxfordshire OX11 0DE, U.K.

<sup>⊗</sup>Department of Chemistry, State University of New York at Stony Brook, Stony Brook, New York 11794-3400, United States

## S Supporting Information

**ABSTRACT:** Nanosized, carbon-coated  $\text{LiFePO}_4$  (LFP) is a promising cathode for Li-ion batteries. However, nano-particles are problematic for electrode design, optimized electrodes requiring high tap densities, good electronic wiring, and a low tortuosity for efficient Li diffusion in the electrolyte in between the solid particles, conditions that are difficult to achieve simultaneously. Using *in situ* energy-dispersive X-ray diffraction, we map the evolution of the inhomogeneous electrochemical reaction in LFP-electrodes. On the first cycle, the dynamics are limited by Li diffusion in the electrolyte at a cycle rate of C/7. On the second cycle, there appear to be two rate-limiting processes: Li diffusion in the electrolyte and electronic conductivity through the electrode. Three-dimensional modeling based on porous electrode theory shows that this change in dynamics can be reproduced by reducing the electronic conductivity of the composite electrode by a factor of 8 compared to the first cycle. The poorer electronic wiring could result from the expansion and contraction of the particles upon cycling and/or the formation of a solid-electrolyte interphase layer. A lag was also observed perpendicular to the direction of the current: the LFP particles at the edges of the cathode reacted preferentially to those in the middle, owing to the closer proximity to the electrolyte source. Simulations show that, at low charge rates, the reaction becomes more uniformly distributed across the electrode as the porosity or the width of the particle-size distribution is increased. However, at higher rates, the reaction becomes less uniform and independent of the particle-size distribution.



## ■ INTRODUCTION

There is considerable motivation to develop much larger Li-ion batteries, with increased rate performance and cycle life, particularly for use in electric vehicles and for grid storage, batteries being used in this latter application to balance demand with supply, allowing the increased use of intermittent renewable sources.  $\text{LiFePO}_4$  (LFP)<sup>1</sup> is one of the most promising cathode materials for these applications, due to its low toxicity, good reversibility, and thermal stability.<sup>2</sup> However, it has very low ionic and electronic conductivity<sup>1,3</sup> and is prone to antisite defects (the presence of Fe on the Li site and vice versa)<sup>4</sup> that block the one-dimensional (1D) diffusion channels, reducing the number of accessible Li-ions in the lattice. LFP's performance in an electrode was found to be significantly improved by decreasing the particle size<sup>5,6</sup> and by the addition of a carbon coating.<sup>7,8</sup> Nano-LFP particles have been shown to exhibit good capacities at exceptionally high discharge rates,<sup>2,9</sup> compared to micron-sized LFP particles and other Li-ion cathode materials. Other routes to increased rate performance have, for example, included the synthesis of hierarchical LFP

particles (for example, microflowers<sup>10</sup>) and the use of cation substituted materials (e.g., cupric- and vanadium-substituted  $\text{LiFePO}_4$ <sup>11–13</sup>).

Various models have been proposed to explain LFP's high-rate capability at the single particle level. These include the mosaic instability,<sup>14</sup> domino-cascade,<sup>15</sup> and metastable solid solution<sup>16</sup> models. The latter mechanism was originally proposed on the basis of first-principles calculations<sup>16</sup> but has been recently verified experimentally by using *in situ* X-ray diffraction studies.<sup>17,18</sup> All these models predict sequential, particle-by-particle reactions at low currents and, critically, have significant implications for the reaction mechanism at the electrode-level.

In 2010, Liu et al.<sup>19</sup> used *ex situ* microdiffraction to study a partially charged LFP battery and show that delithiation does not occur homogeneously through the electrode. The reaction

Received: November 24, 2014

Revised: February 13, 2015

Published: February 27, 2015

preferentially occurs closer to the separator than to the current collector, indicating that Li-ion transport in the electrolyte within the electrode pores is kinetically limiting. These experiments were carried out at high charge rates and showed that although the nanosized LFP particles themselves can handle high discharge rates, the limitations of the Li diffusion through the electrode presumably prevent the full capacity from being achieved at high rates. More recently, Robert et al.<sup>20</sup> carried out *ex situ* experiments on the LFP-electrode using transmission electron microscopy and electron forward scattering diffraction and observed a “stratum by stratum” progression of the LFP electrochemical reaction through the electrodes. After 60 cycles, unreacted particles were typically found furthest away from the separator (near the current collector). These results suggest that the loss of capacity in extended cycles is due to particles that are no longer accessible to the electrolyte. Ouvrard et al.<sup>21</sup> used *in situ* X-ray absorption spectroscopy to study the inhomogeneity of the LFP reaction in the plane of the electrode perpendicular to the applied current in a modified “Swagelok-type” battery.<sup>22</sup> They observed a tendency of particles to react near the edges of the electrode rather than near the center. However, the most notable inhomogeneity was at the center of the electrode, at the same position as the X-ray window (i.e., the hole in the stainless steel that allows the incoming X-ray beam to penetrate the electrode). The significant inhomogeneity was, therefore, attributed to the lower pressure in the center as compared with the edges, owing to the gap between the electrode and the X-ray window (in this case, a beryllium disk).

Several modeling and simulation studies were conducted to explore these issues. Johns et al.<sup>23</sup> introduced the sharp discharge front model to describe Li diffusion in a porous electrode at different charge rates. Roberts et al.<sup>24</sup> quantified the proportion of the electrode that is accessible to the Li-ions in high charge rates and applied it to an LFP-battery. Orvananos et al.<sup>25</sup> carried out simulations of an electrode containing same-size particles to analyze the dependence of transformation on the particle position. Van der Ven and Wagemaker<sup>34</sup> studied the effect of surface curvature (varying as a function of particle shape and size) on the reaction mechanism, while Cogswell and Bazant<sup>27</sup> considered the wetting of the particles' surfaces. Orvananos et al.<sup>28</sup> also studied the effect of particle size and connectivity between particles on the phase transformation behavior of LFP-electrodes. However, the combined effect of both particle position within the electrode and particle-size distribution has not yet been studied experimentally and theoretically.

More generally, the rate performance of a practical battery, and the reaction mechanism, is not just a function of the size and morphology of the active materials but as the above studies demonstrate, depends strongly on the structure of composite electrode and the resulting electronic and ionic conductivities. Several experimental studies have shown noticeable improvements to the electrochemical performance by using electrode designs that enhance the electrode kinetics. A dual-scale porous structure, with overall decreased tortuosity, was developed by Bae et al.<sup>29</sup> on the model material,  $\text{LiCoO}_2$ . It consisted of large channels to act as the main Li transport routes over the length of the electrode and finer pores for diffusion on smaller length scales. In another study, Fongy et al.<sup>30</sup> improved the electrochemical behavior, by using carbon fibers that facilitated both the ionic and electronic conductivity through the cathode. Ebner et al. have, more recently, correlated the anisotropic

tortuosity in composite electrodes with the shape of the constituent particles in the electrodes.<sup>31</sup> Their study demonstrated that the rate performance can be improved by up to a factor of 4, by reducing the tortuosity through the use of spherical graphite particles or by aligning platelet-shaped particles.<sup>31</sup>

These studies all highlight the need to understand the relationship between reaction mechanisms at the particle and whole electrode level and to use this understanding to optimize performance. Toward this goal, the development of new synchrotron-based techniques has been instrumental in generating new insight into the electrochemical processes that occur in batteries. While energy-dispersive X-ray diffraction (EDXRD) is more commonly known for being highly effective for strain and phase mapping in engineering applications,<sup>32–34</sup> we and others have developed it to study reactions in intact coin cells.<sup>35,36</sup> For example, the method was applied successfully to study the lithiation mechanisms that occur in lithium–silver–vanadium–phosphorus-oxide batteries.<sup>37,38</sup> The high-energy X-rays are able to penetrate the stainless steel casing of a coin cell battery to monitor the electrochemical reaction occurring inside a commercial-type battery. The method is advantageous over other transmission-based diffraction experiments because it does not require a special cell design that might alter the way the electrode performs and/or lower the performance, which would raise questions as to whether the results are inherent to the materials rather than the cell design. Unlike the destructive *ex situ* approach, *in situ* experiments allow the reaction to be monitored throughout the cycling process.

In this study we monitored the phase evolution in an LFP-electrode in a coin cell battery using *in situ* EDXRD, and combined this with three-dimensional (3D) porous electrode simulations, in order to determine the physical origins of the inhomogeneity seen in LFP-electrodes. The EDXRD experiments utilized the narrow slit size at beamline I12 at the Diamond Light Source to collect 1D maps simultaneously in two different directions of the electrode as the battery was cycled. Collimators between the sample and detector define a gauge volume at the sample position, so that only diffraction signals inside that volume reach the detector. By moving the battery on a motorized stage, different positions within the battery can be studied, both across and through the cathode. The simulation results are used to elucidate the effect of particle position on the electrochemical dynamics of the electrode. By combining the results from the EDXRD experiments and 3D simulations, we monitor the progression of the electrochemical reaction through the electrode over two cycles and explore the parameters that affect differences in the extent of reaction across the LFP-electrode. We show that both the electronic and the ionic conductivity through the electrode control the reaction progression through the electrode.

## ■ EXPERIMENTAL AND SIMULATION DETAILS

**Synthesis and Characterization.** Carbon-coated LFP (C-LFP) was synthesized via the solid-state method<sup>39</sup> using iron oxalate (Sigma-Aldrich, 99%), lithium carbonate (Sigma-Aldrich, 99.997%), ammonium dihydrogen phosphate (Sigma-Aldrich, 99.999%), and 10 wt % Ketjen black (AzkoNobel) in a stoichiometric mixture. After high-energy ball milling for 20 min, the reaction mixture was pelletized and heated to 600 °C under flowing argon for 6 h.

Laboratory X-ray diffraction was performed to confirm the purity of the as-synthesized material with a PANalytical Empyrean X-ray diffractometer with a  $\text{Cu K}\alpha$  source. The total scan time was 9 h

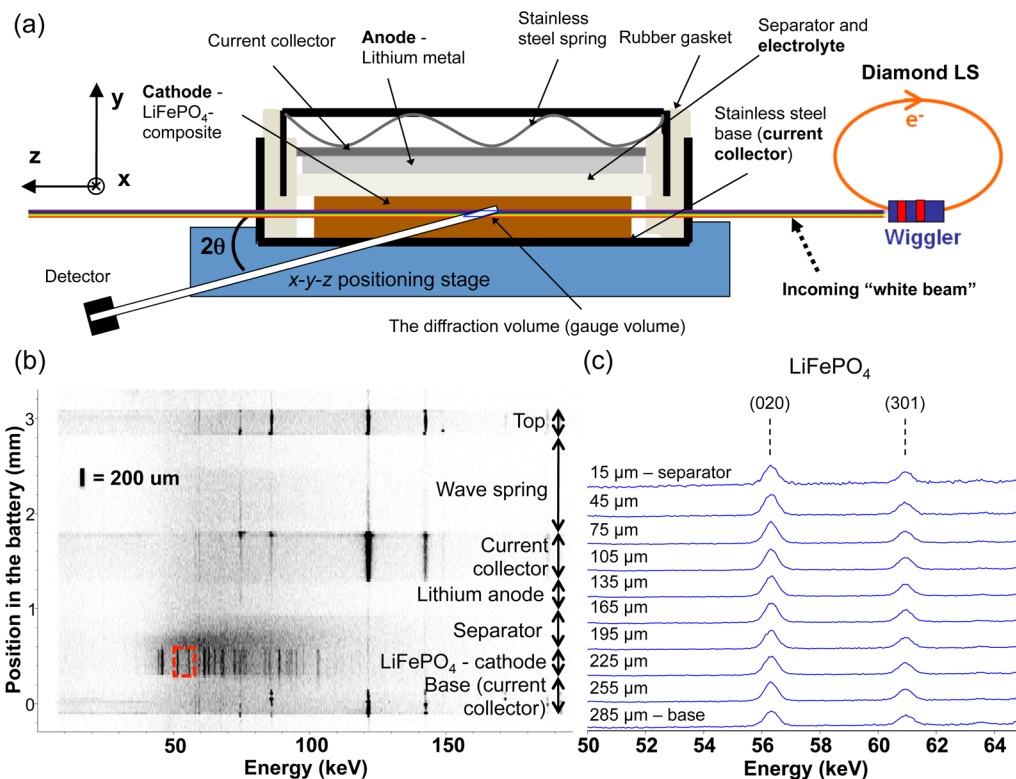


**Figure 1.** (a) *In situ* EDXRD setup at the Diamond Light Source and the cross section of a coin cell battery placed on an *x-y-z* positioning stage. The X-rays penetrate the stainless steel casing and the diffracted X-rays are detected at a fixed angle. (b) A diffraction intensity plot (versus position in the battery) of the EDXRD patterns for the whole coin cell, in which the LFP-cathode can clearly be seen above the base, the base also acting as the current collector at the cathode. The diffraction patterns inside the red box in part b (the 50–65 keV region) are shown as slices in part c and labeled with respect to the distance from the separator. This region, which contains the (020) and (301) reflections is displayed in subsequent plots, although the full profile with the full energy window is used in all the Rietveld analyses.

and 52 min using a step size of  $0.017^\circ$  over a  $2\theta$  range from 5 to  $140^\circ$ . TOPAS software<sup>40</sup> was used to perform a Rietveld refinement on the as-synthesized powder.

**Film Fabrication and Battery Assembly.** The electrode was prepared by grinding 85 wt % C-LFP, 10 wt % carbon nanofibers, and 5 wt % polytetrafluoroethylene (PTFE) (the latter two from Sigma-Aldrich) in a mortar and pestle, until the mixture came together and became shiny in appearance. The mixture was then rolled into a 300- $\mu\text{m}$  film. A circular punch, 7/16 in. (11.1 mm) in diameter, was used to cut the cathode (27.9 mg). A coin-cell-type battery was assembled in an argon-filled glovebox, using Li metal as the counter electrode, a Whatman GF/B borosilicate microfiber filter as the separator and 1 M  $\text{LiPF}_6$  solution in a 1:1 mixture of ethylene carbonate/dimethyl carbonate as the electrolyte.

**EDXRD.** The EDXRD experiments were conducted at the Diamond Light Source (U.K.) on the superconducting wiggler beamline, I12. “White beam” radiation was used, the beam being  $300\ \mu\text{m} \times 30\ \mu\text{m}$  in size in the *x*- and *y*-directions, respectively (defined by the slit sizes employed for the incoming beam). The intensity of the diffracted beam versus momentum transfer (*q*) was measured using 23 germanium detectors spaced azimuthally at  $8.1818^\circ$ . The *q* calibration for each detector was performed using diffraction data collected from a NIST 674b cerium oxide powder sample. Detector channel 21 showed poor resolution due to high leakage current, so it was disregarded in the analysis. The remaining 22 detectors were interpolated using splines (with number of knots, *k* = 5) so that the data from the 22 detectors could be summed in *q*. This was then converted into energy, *E*, using the following equation:

$$E = (hc \times q) / (4\pi \sin \theta) \quad (1)$$

where *h* is Planck’s constant, *c* is the speed of light, and  $\theta$  is half the angle subtended by the incident beam and the lattice planes. Similar

experiments were also performed at the National Synchrotron Light Source (NSLS) at Brookhaven National Laboratory (see the Supporting Information).

**EDXRD Experiments and Refinements.** The cross section of the coin cell battery and the experimental setup at I12 is shown in Figure 1a. An X-ray diffraction (XRD) 1D map of the battery was first performed by collecting energy-dispersive XRD patterns in 30  $\mu\text{m}$  steps in the *y*-direction, at *x* = 0 (approximately the center of the cell) (Figure 1b) so as to determine the locations of the different components in the battery (and more specifically, to locate the active material, LFP). An enlargement showing key LFP reflections is shown in Figure 1c. Two sets of 1D maps were then performed during electrochemical cycling to measure the extent of reaction in both the *y*- and *x*-directions. In total, an 11 mm-wide region is mapped in the *x*-direction using a step size of 1 mm, and a 300- $\mu\text{m}$ -deep region is mapped in the *y*-direction using a step size of 30  $\mu\text{m}$ . Note that the minimum step-size is constrained by the size of the beam.

Structural refinements of the energy-dispersive X-ray diffraction (XRD) patterns are more challenging than for the more commonly studied, angular-dispersive XRD patterns. Full Rietveld analysis on EDXRD data was carried out by Scarlett et al.,<sup>41</sup> by considering the absorption of every component the X-ray beam travels through, and the distance travelled by the beam through these components, to account for the final intensities observed in the diffraction pattern. For this study, since each position in the battery has a unique pathway for the incident and scattered beam, it requires a different absorption correction. A full Rietveld refinement on the diffraction data would involve an absorption analysis of all the coin-cell components that the beam passes through (i.e., steel casing, carbon, PTFE binder, and the electrolyte, in addition to LFP/FePO<sub>4</sub> (FP)). Thus, we adopted a simpler approach to model the intensity variation and used a modified-Rietveld refinement procedure for the diffraction patterns to extract



the LFP and FP phase fractions at the different positions (in both  $x$  and  $y$ ) in the battery.

At first, the LFP pattern at the beginning of the charge was refined: all the structure parameters were fixed; then the unit-cell parameters, atom-site positions and thermal parameters were sequentially refined. This refinement procedure was repeated for each layer within the electrode. The same refinements were then carried out for FP at the end of the charge, where the FP content was maximum, for all the layers. Subsequently, all the LFP and FP parameters were fixed for each layer, to account for the differences in intensity distribution due to the path of the beam, and only the scale factors of the LFP and FP phases were refined during cycling. The parameters obtained for the LFP and FP phases from the beginning and end of the charge, respectively, were used to refine the patterns when there was approximately 50% LFP and 50% of FP observed in the pattern (i.e., at a capacity corresponding to approximately  $\text{Li}_{0.5}\text{FePO}_4$  on the charge and also for the discharge) to validate the approach. Sequential refinements of the LFP and FP phase fractions were subsequently carried out for increasing and decreasing LFP content, layer by layer. This approach resulted in reasonable fits with the experimental diffraction patterns (see the Supporting Information). Implicit in this analysis is the assumption that the sum of the phase fractions is equal to one for each pattern. This assumption is valid at slow rates, as shown by Chueh et al.,<sup>42</sup> at a cycle rate of 1C, in which only 2% of the particles were found to be undergoing phase transformation at a time and the other 98% were either nearly fully lithiated or nearly fully delithiated. However, the results by Liu et al. show that this is not true at high rates<sup>17</sup> and therefore we would need to develop a more sophisticated model to perform higher rate studies. Even though the atomic positions and thermal parameters extracted from this study are not reliable, the output of the phase fraction of LFP and FP within each pattern should be as the distortion to the peaks for each phase has been accounted for and is consistent through the cycle. A comparison of the depths of discharge (DODs, i.e., % overall lithiated) from the bulk electrochemistry and the DOD from the EDXRD refinements is shown in Figure S3 of the Supporting Information and is discussed in the next section.

**Porous Electrode Simulations.** Porous electrode theory<sup>43,44</sup> is used to model the discharge of the cell described above. Unlike simple porous electrode models, in which only the average size is employed, this model accounts for the particle-size distribution.<sup>45,46</sup> Five coupled equations are solved to predict the concentration evolution during discharge of the cell. They describe (1) concentration evolution and (2) current continuity in the electrolyte, (3) concentration evolution and (4) current continuity in the porous electrode, and (5) electrochemical reaction. We consider three relevant phases for this system: active material (LFP), inactive material (carbon and PTFE), and electrolyte. A domain geometry that approximates the experimental cell was employed. Figure 2 shows the configuration of the simulation. The casing, which is a cylinder in the experiment, is represented in the simulation by a square prism with the same volume. This approximation is appropriate because, as shown in the results, we do not observe significant gradients in the electrolyte domain on the sides of the cathode. The governing equation, parameters, and the remainder of the simulation details can be found in the Supporting Information.

## RESULTS AND DISCUSSION

### Synthesis and Characterization of the LFP-Electrodes.

Carbon-coated LFP (C-LFP), space group  $Pnma$ , was synthesized via solid-state synthesis and was confirmed to be single phase using XRD (see the Supporting Information). A Rietveld refinement was carried out on the XRD pattern, and the following lattice parameters were extracted:  $a = 10.3252$  ( $\pm 0.0004$ ) Å,  $b = 6.0056$  ( $\pm 0.0002$ ) Å,  $c = 4.6932$  ( $\pm 0.0002$ ) Å, and volume =  $291.02$  ( $\pm 0.02$ ) Å<sup>3</sup> (the errors corresponding to the standard uncertainties obtained from the Rietveld analysis).

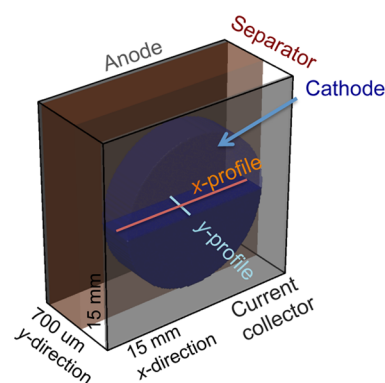


**Figure 2.** Simulation configuration. A cylindrical cathode with the same dimensions as the experimental cell is simulated. The lines noted by “x-profile” and “y-profile” indicate the lines along which the measurements are assumed to be made. The figure is not to scale; the  $y$ -direction is magnified by a factor of 10.

These values agree well with the literature<sup>39</sup> and suggest that there are negligible antisite defects in the particles.<sup>4</sup>

The C-LFP particles were made into a thin-film electrode using either PTFE or PVDF as the binder and carbon nanofibers (CNF) as the conductive carbon matrix. CNFs were used to create a 3D matrix with good electronic and ionic conductivity. The latter is thought to arise from the electrolyte-filled porous channels that are created parallel to the fibers.<sup>30</sup>

Scanning electron microscopy (SEM) images of the LFP-PTFE electrode show that the LFP particles adopt a spherical-type morphology with a large distribution of particle sizes (see Figure S5, Supporting Information), both of which are expected for the solid-state synthesis route.<sup>47,48</sup> Fifty particles were sampled at different scales of magnification, and the average and median particle sizes were calculated to be 122 and 110 nm in diameter, respectively. The particle-size range was 43–340 nm (most particles falling within 50–250 nm) as seen in the analysis shown in Figure S6 in the Supporting Information. The SEM images clearly show an electrode structure that leads to hierarchical electronic conductivity across the electrode. On the micron-scale the electronic conductivity will be dominated by the CNFs, whereas on the nanoscale, the electronic conductivity will be primarily via the carbon coating of the LFP particles and relies on good particle connectivity. Pores of  $\sim 750$  nm can be seen; however, the majority appear to be  $<100$  nm. The Brunauer–Emmett–Teller (BET) results show that the electrode has a large BET surface area of  $76.5 \text{ m}^2/\text{g}$  ( $\pm 1.4 \text{ m}^2/\text{g}$ ),<sup>49,50</sup> a Barrett–Joyner–Halenda (BJH) adsorption cumulative pore volume of  $0.25 \text{ cm}^3/\text{g}$ , and a BJH adsorption average pore diameter of 12 nm. The average pore diameter is smaller than the resolution of the SEM, but since the diameter is an order of magnitude larger than the size of the  $\text{Li}^+$  solvation shell in the electrolyte,<sup>51</sup> there should be efficient transport of the ions through the channels. The pores occupy 24% of the total electrode volume (the calculation is shown in the Supporting Information) and are the primary transport pathway for the Li-ions.

**EDXRD on Coin Cell Batteries and Porous Electrode Simulations. Optimization of the Electrode Composition.** In the EDXRD experiments, the X-rays exit through the stainless steel casing of a standard coin cell battery (Figure 1a), the casing acting as an absorber; therefore, it is critical to ensure that the diffraction signal from the LFP particles is above the minimum detection threshold. The first experiments at the

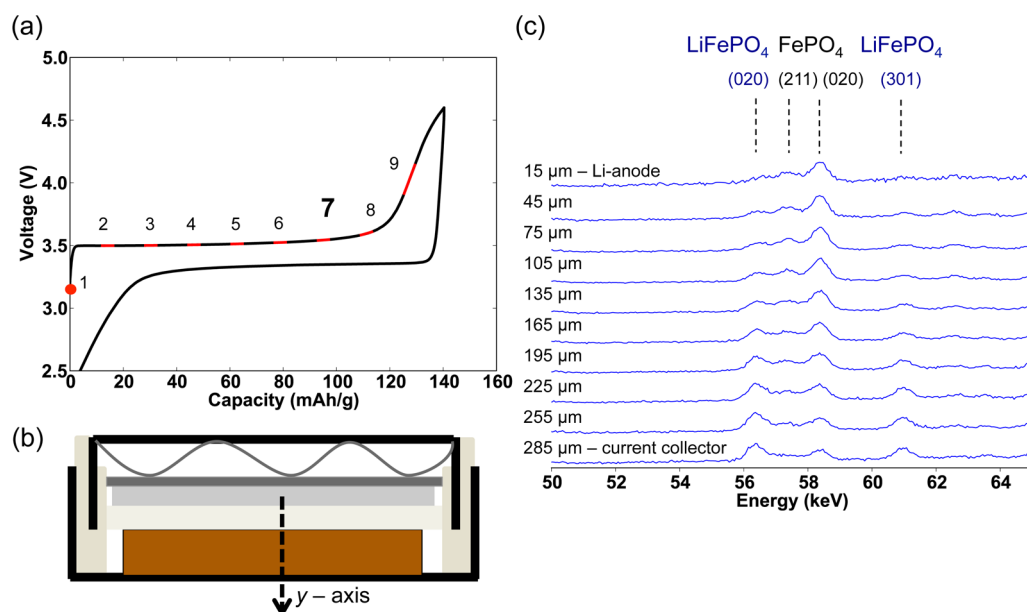


**Figure 3.** *y*-Profiling at a charge rate of C/7 on the first cycle. A set of diffraction patterns was collected during time segments marked by red on the voltage curve (a). For each measurement, 10 positions through the cathode were profiled at different depths in the *y*-direction (b), as marked in part c. The diffraction patterns at scan no. 7 are shown in part c.

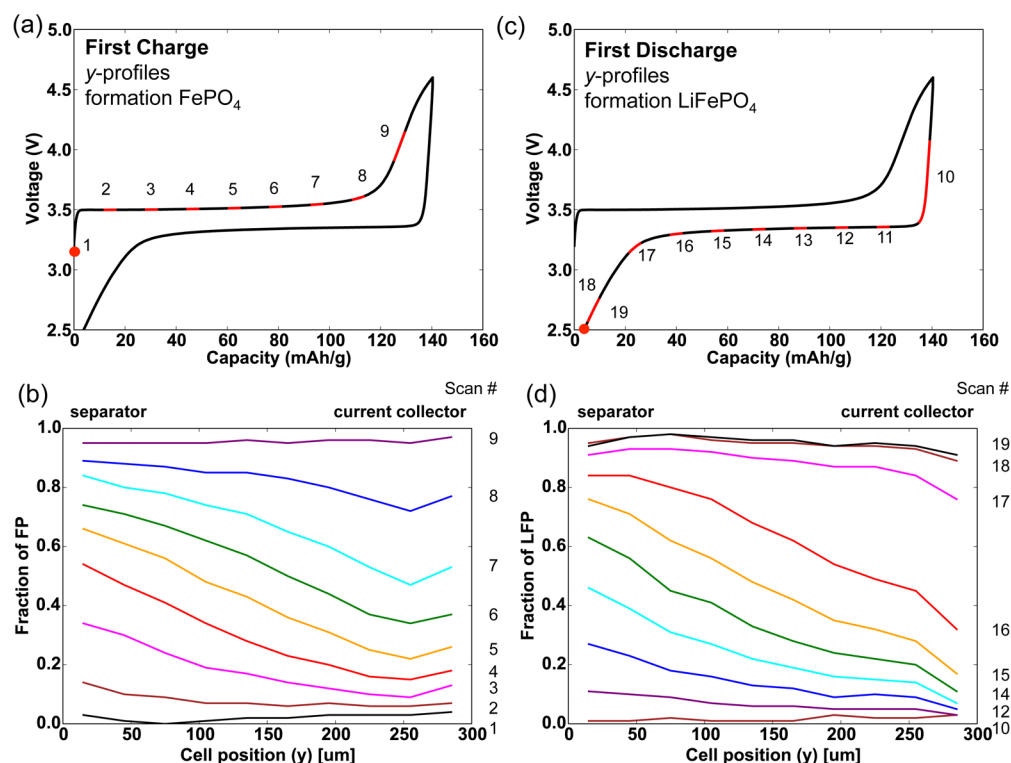


**Figure 4.** *y*-Profiling upon (a, b) charge and (c, d) discharge in a battery cycling at a charge rate of C/7 on the first cycle. Parts a and c show the voltage as a function of the capacity. The phase fraction of (b) FP that forms upon charging is plotted as a function of position in the cell, where 15 and 285  $\mu\text{m}$  are the center of the beam closest to the separator and next to the current collector, respectively. (d) The evolution of the formation of LFP upon discharging the battery.

Diamond Light Source used polyvinylidene fluoride (PVDF) as the binder, but negligible diffraction signal was observed from LFP, presumably due to the lower density of LFP/PVDF composite electrodes. In contrast, the PTFE-based electrode films have a high density of LFP particles and therefore the diffraction signal from LFP is stronger and more signal

penetrates through the stainless steel casing allowing diffraction patterns with good signal-to-noise to be collected in reasonable time periods (Figure 1c). The PTFE electrodes can also handle higher rates, and hence, thicker (300- $\mu\text{m}$ ) electrodes could be prepared, allowing us to obtain more sampling points in the *y*-direction. The reaction front can thus be monitored with high

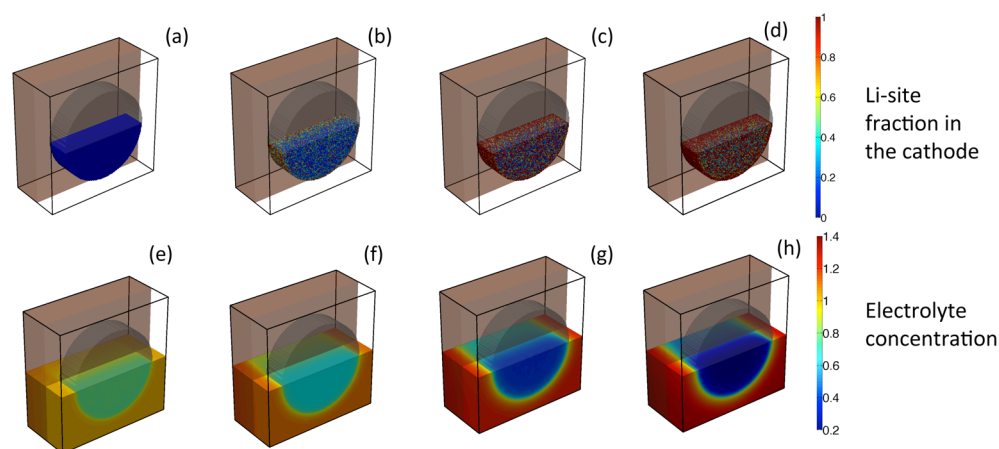


**Figure 5.** Discharge simulation for the first cycle. (a–d) Li concentration in the electrode, at (a) 7% DOD, (b) 24% DOD, (c) 47% DOD, and (d) 63% DOD. Here, the color bar represents the Li site fraction. (e–h) The electrolyte concentration at the same set of DODs. The color bar indicates the molarity of the Li ion.

resolution. A thinner, LFP/PVDF composite film was also prepared and profiled at the NSLS during the first charge/discharge cycle. The results were qualitatively similar (as shown in the Supporting Information) to those obtained for the PTFE based electrodes. However, as more data points can be collected in the thicker electrodes, the PTFE-based film is explored in more detail in this paper.

**Depth (*y*)-Profiling through the Electrode.** EDXRD of the LFP-PTFE cathode in a standard coin cell battery was performed with the coin cell fixed to an *x*-*y*-*z*-positioning stage, as shown in Figure 1a. The axes definition employed at the synchrotron is used in this study to define the *x*-, *y*-, and *z*-directions. The +*z*-direction is the direction of the incoming beam; +*y* is defined such that it is perpendicular to the circular face of the coin cell and pointing in the direction from the cathode to the anode, and +*x* is the direction orthogonal to the *y*- and *z*-axes and is through the center of the coin cell. We collected EDXRD patterns through the depth of the entire coin cell (*y*-direction) before cycling the battery to demonstrate the imaging capabilities of EDXRD and determine the location of the different components (see Figure 1b). The strong diffraction signals from the stainless steel base, current collector, and top are clearly observed. The LFP-electrode is readily recognized by the many reflections that are characteristic to the LFP crystal structure and its larger unit cell volume in comparison to steel. The separator has no distinct reflections and is observed as an amorphous, broad signal. The Li metal anode, despite being crystalline, has no observable diffraction peaks, as Li diffracts very weakly and either the signal does not penetrate the casing of the coin cell or the polycrystalline Li metal foil gives discrete diffraction spots rather than rings, causing the Bragg peak to occur outside the detector.

**First Cycle.** The results from the *in situ y*-profiling of the electrode at a charge and discharge rate of  $C/7$  (7 h to charge and 7 h to discharge) are shown in Figures 3 and 4. A total of 19 profiles were recorded at different depths of the electrode at each stage of the charge/discharge cycle. A single XRD pattern for one layer took 60 s to record; therefore, a set of diffraction patterns through all 10 profiles at different depths took 10 min. The periods over which the data is collected are marked in red in the voltage profile in Figures 3a, and 4a, 4c. We cycled the battery at a moderately low rate so that the change in Li content in the electrode between the 10 depths was negligible;

in the 10 min that the measurements were taken, there is a 2.3% change in the total Li content in the electrode. Both the slit and step size in the *y*-direction were 0.03 mm; therefore, the measurements covered the entire depth of the electrode (0.3 mm). The discharge capacity was 137 mAh/g, which represents 81% of the total theoretical capacity for LFP.<sup>5</sup> The reversible capacity was lower than in previous LFP studies, suggesting that the electrode is not fully optimized for LFP, probably due to the large thickness of the electrodes used in this study.

First, we examine the 10 diffraction patterns taken through the cathode on the first charge, at scan no. 7, shown in Figure 3c. In the layers closer to the separator and the Li anode, the FP (211)(020) reflections are stronger than the LFP (020) reflections, whereas the LFP peaks are more intense closer to the current collector (i.e., the stainless steel base). This trend demonstrates that the  $\text{LiFePO}_4 \rightarrow \text{FePO}_4 + \text{Li}^+$  electrochemical reaction occurs preferentially in the particles that are closer to the separator than to the current collector. The inhomogeneity of the electrochemical reaction in the electrode suggests Li-diffusion limited-kinetics in the electrolyte across the cathode,<sup>52</sup> which is in agreement with the *ex situ* depth profiling performed by Liu et al.<sup>19</sup>

The results from the modified-Rietveld refinements carried out on the diffraction patterns for both the charge and discharge are shown in Figure 4 (the data plotted with error bars extracted from the refinements are shown in the Supporting Information). For the charge and discharge, the evolution of the product (i.e., FP and LFP, respectively) is plotted as a function of position in the electrode measured from the separator. Both intercalation into and deintercalation from the Li cathode appear to be controlled by similar limitations, as the behavior seen on charge and discharge are similar. As shown qualitatively in Figure 3c, the onset of reaction is faster at a depth of 15  $\mu\text{m}$  (i.e., next to the separator), compared with 285  $\mu\text{m}$  (next to the current collector). There is a discontinuity between 255 and 285  $\mu\text{m}$  on charge (Figure 4b), which may be attributed to the close proximity of the particles to the current collector at 285  $\mu\text{m}$ , where electrons are readily available. This means that there is slight preference for LFP particles closer to the current collector to react than those 30  $\mu\text{m}$  away, and in this narrow region the better wiring ensures more rapid delithiation. The gradient of Li content in the LFP particles at scans no. 4–7 during charging is 1.6 Li fraction/mm (Figure

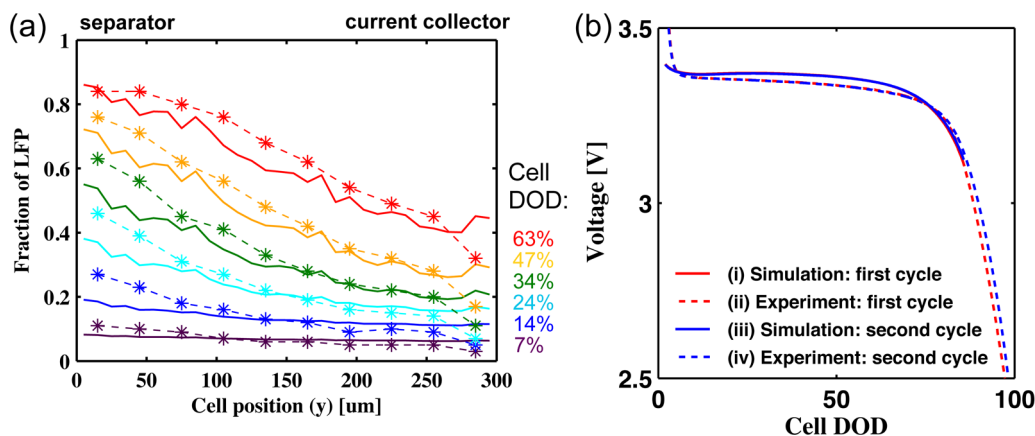


**Figure 6.** (a) Fraction of LFP in the  $y$ -profile for the first discharge. The solid lines indicate the simulation results, and the dashed lines with markers indicate the experimental results. (b) Comparison of the experimental and simulated voltages from the first and second discharges.

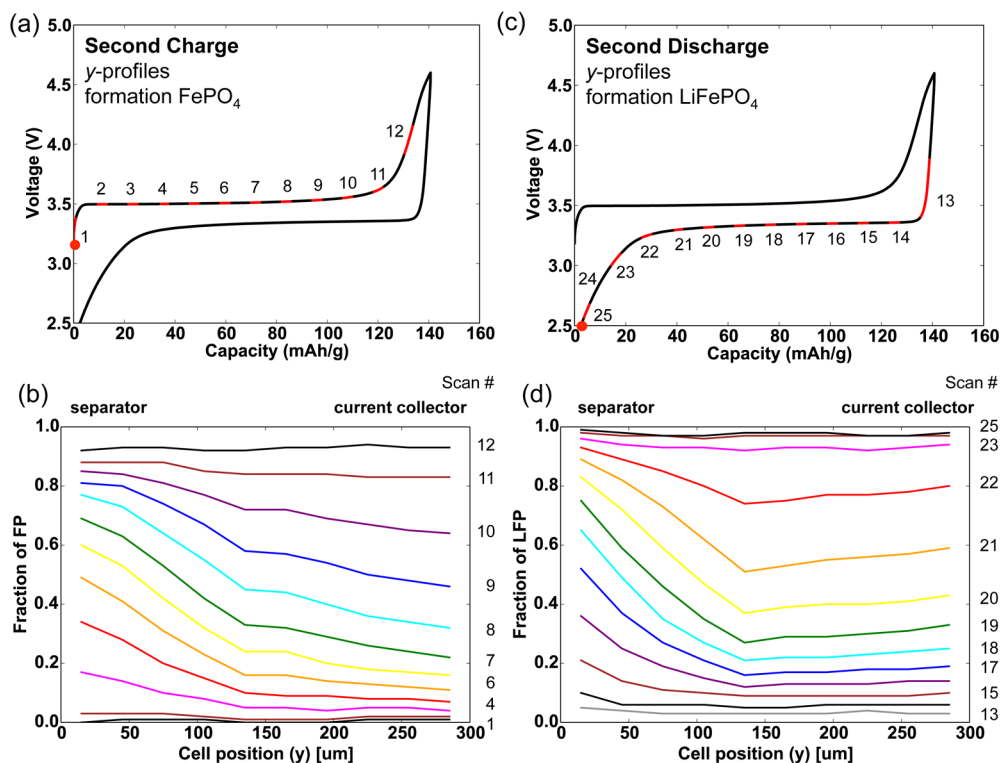


**Figure 7.**  $y$ -Profiling upon (a,b) charge and (c,d) discharge at a  $C/7$  rate on the second cycle. Parts a, and c show the voltage as a function of the capacity. The phase fraction of (b) FP that forms upon charging is plotted as a function of position in the cell, where  $15\ \mu\text{m}$  is the center of the beam closest to the Li anode and electrolyte. (d) The evolution of the formation of LFP upon discharging the battery. A total of 25 scans were performed during the second cycle by sampling more frequently than in the first cycle (which has 19).

4b), while upon discharge (Figure 4d), the gradient at scans no. 13–16 is slightly steeper ( $1.8\ \text{Li fraction/mm}$ ). The same experiment was carried out for a PVDF electrode and also shows the reaction occurring preferentially in the LFP particles closest to the Li anode, rather than near the stainless steel current collector (this data is shown in the Supporting Information).

The simulation results for the first discharge (lithiation) are shown in Figure 5. (The model was parametrized for the discharge process only, and therefore the charge process was not considered in this paper.) Figure 5a–d shows four snapshots of the concentration evolution. As in the experiments, the first particles to lithiate are closest to the Li anode.

We also observe that the particles closest to the circular side react before those in the center. Figures 5e–h show the concentration of Li salt in the electrolyte at the same DODs. Throughout the process, the electrolyte within the porous cathode becomes gradually depleted as the particles lithiate, reaching a nearly fully depleted state near the end of the process, even though these experiments were performed at a relatively slow rate ( $C/7$ ). In the meantime, Li ions are released from the anode to the electrolyte to conserve the electrolytic charge; therefore, the Li concentration outside the porous electrode increases.

The reaction evolution in the  $y$ -direction is shown in Figure 6a at six different DODs for both the simulation and the



experimental results. The two sets of results are in good agreement: the slope and the trend match well, and the values are also close for the most part. For the profile comparisons, the average DOD of the profile is considered representative of the average DOD of the cell and is used to compare the experiment and simulations. The differences between the DODs from the EDXRD experiments and the porous electrode simulations are shown in Table S1 in the Supporting Information. The fluctuation in the fraction of LFP observed in the simulation profiles are caused by the relatively small number of particles employed to represent the particle-size distribution. The voltages for the simulation and the experiment are shown in Figure 6b, curves i and ii, respectively. The simulation and the experiment have similar capacities and, in agreement with the experiment, the simulated cell potential decreases at a DOD of  $\sim 75\%$ . However, the simulated voltage is higher than the experimental voltage (by  $\sim 10\text{--}20\text{ mV}$ ). This difference can be attributed to the several simplifications in the porous electrode model, such as the assumption of electroneutrality in the electrolyte, the lack of consideration of particle contact or other geometrical effects, as well as concentration inhomogeneity within the particles in the pseudocapacitor model and the simplified model for reaction.

**Second Cycle.** The battery was cycled for a second time at C/7 after a 24-h rest. During the second cycle, another set of the  $y$ -profiling data was collected. The results are appreciably different between the first and second cycles, two (nearly) linear segments are observed in the Li content profile for the second cycle for both charge and discharge (Figure 7). The half of the electrode closer to the separator has a steeper gradient of Li content, while the other half closer to the current collector has a shallower gradient. Upon charge, the gradient of Li content from  $15\text{--}135\text{ }\mu\text{m}$  (i.e., closer to the Li anode/separators) is  $2.7\text{ Li fraction/mm}$ , whereas from  $135\text{--}285\text{ }\mu\text{m}$  (i.e., closer to the current collector) the gradient is significantly smaller ( $0.76\text{ Li fraction/mm}$ ). A similar phenomenon is observed upon discharge, but with an even larger variation in the two gradients:  $3.7\text{ Li fraction/mm}$  over  $15\text{--}135\text{ }\mu\text{m}$  and approximately zero over  $135\text{--}285\text{ }\mu\text{m}$ , respectively. Therefore, there seems to be two reaction limitations in this cycle. In the first  $135\text{ }\mu\text{m}$  of the electrode closer to the separator, the behavior is similar to the first cycle and is assumed to be related to Li diffusion limitations in the electrolyte. However, the zero phase-fraction gradients closer to the current collector upon discharging are unexpected and suggest that the electronic conductivity could also be a limiting factor. In this case, the FP particles closer to the current collector lithiate more readily than particles away from the current collector (compare Figure 7d, between  $135\text{--}285\text{ }\mu\text{m}$ ).

A simulation was performed to examine the hypothesis that the effective electronic conductivity is reduced in the second cycle. The configuration and parameters were the same as those used in the simulation of the first cycle, except that the electronic conductivity of the solid components in the electrode was decreased by a factor of 8 as a fitting parameter. Figure 8 shows the  $y$ -profiles predicted by this simulation. In agreement with the experimental results, two segments are observed, one side having a significant gradient and the other nearly flat, which indicates that two limiting factors are playing a role in the second-cycle discharge: the electronic conductivity and the Li diffusion in the electrolyte. When the electronic conductivity becomes a limiting factor, the driving force for reaction of the particles decreases with increasing separation from the current

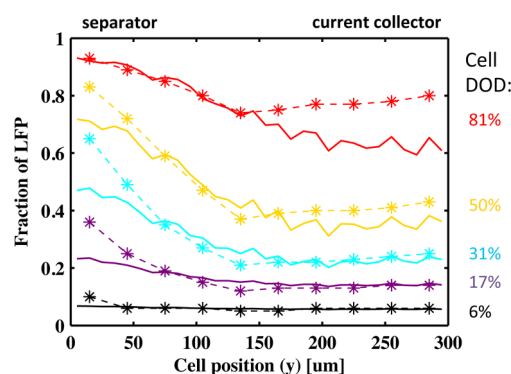


**Figure 8.** Fraction of LFP in the  $y$ -direction for the second discharge. The solid lines indicate the simulation results, and the dashed lines indicate the experimental results.

collector. This limitation offsets the gradient caused by the Li-diffusion in the electrolyte. The resulting voltage for the simulation and the experiment are shown in Figure 6b curves iii and iv, respectively. The voltage is in qualitative agreement with the experimental observation. Despite the decrease in the electronic conductivity, the capacity is comparable to that in the first cycle. Therefore, at these low charge rates, the change in conductivity has a negligible effect on the total number of active particles but instead changes the sequence of reaction of the particles upon cycling and yields a smaller net reaction gradient across the electrode. This decrease in the effective electronic conductivity of the electrode from the first to second cycle is most likely caused by disruptions of the electronic wiring due to the expansion and contraction of the particles upon cycling, which reduce the particle–particle and particle–carbon contacts. Charging was performed to  $4.6\text{ V}$  so it is also possible that the formation of a thin solid-electrolyte interphase (SEI) on the cathode particles contributes to the increased resistance. Although the SEI at the anode is generally considered to be thicker and to impact the internal resistance of the cell more significantly, the role of the cathode SEI is not negligible as some times assumed and should not be completely ignored.<sup>53,54</sup> Future studies will examine the role of the cathode SEI in greater detail.

**Lateral ( $x$ )-Profiling Across the Electrode.** In addition to the  $y$ -direction, we profiled in the  $x$ -direction (i.e., the profile across the electrode Figure 1a) during the second cycle ( $x$ -profiling was not performed for the first cycle). The slit size in  $x$  was  $0.3\text{ mm}$  and 12 diffraction patterns were taken  $1\text{ mm}$  apart. The EDXRD patterns at scan no. 9 on the charge (Figure 9c) show that there is more FP than LFP near the edges ( $x = 5.5\text{ mm}$  and  $x = -5.5\text{ mm}$ ) compared to the center of the cathode (here,  $x = 0\text{ mm}$  is defined as the center of the electrode).

The modified Rietveld refinements were carried out on all the patterns for the second cycle (Figure 10). In Figure 10b,d, the reaction profile has a “cup”-like appearance, with the particles at the sides reacting faster than those in the central region of the cathode. The first  $2\text{ mm}$  of the electrode from the edges to the center on the left-hand-side has a gradient of  $0.11$  and  $0.09\text{ Li fraction/mm}$  upon charge and discharge, respectively. This is the steepest gradient in the  $x$ -direction and is 14 and 20 times smaller than the gradient of Li content observed in the  $y$ -profiling (parallel to the applied current) during the first charge and discharge, respectively. Therefore, in the  $x$ -direction, Li-diffusion-limited kinetics leads to a concentration gradient in the electrolyte due to the edges of



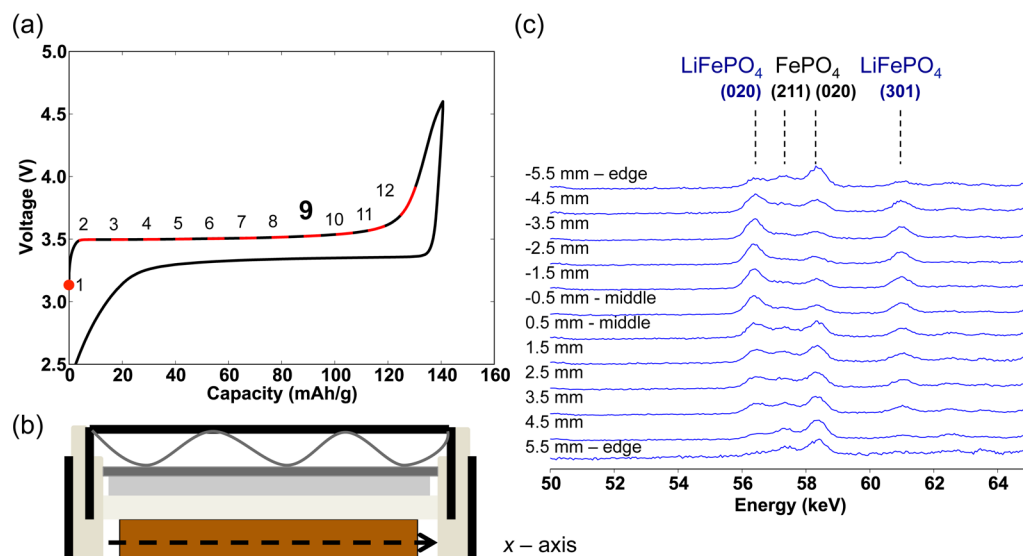


**Figure 9.** *x*-Profiling at a charge rate of  $C/7$  on the second cycle. A set of diffraction patterns was collected during time segments marked by red on the voltage curve (a). For each measurement, 12 positions across the cathode were profiled along the *x*-direction, marked by the dashed arrow in part b. The diffraction patterns at scan no. 9 on the second cycle are shown in part c.

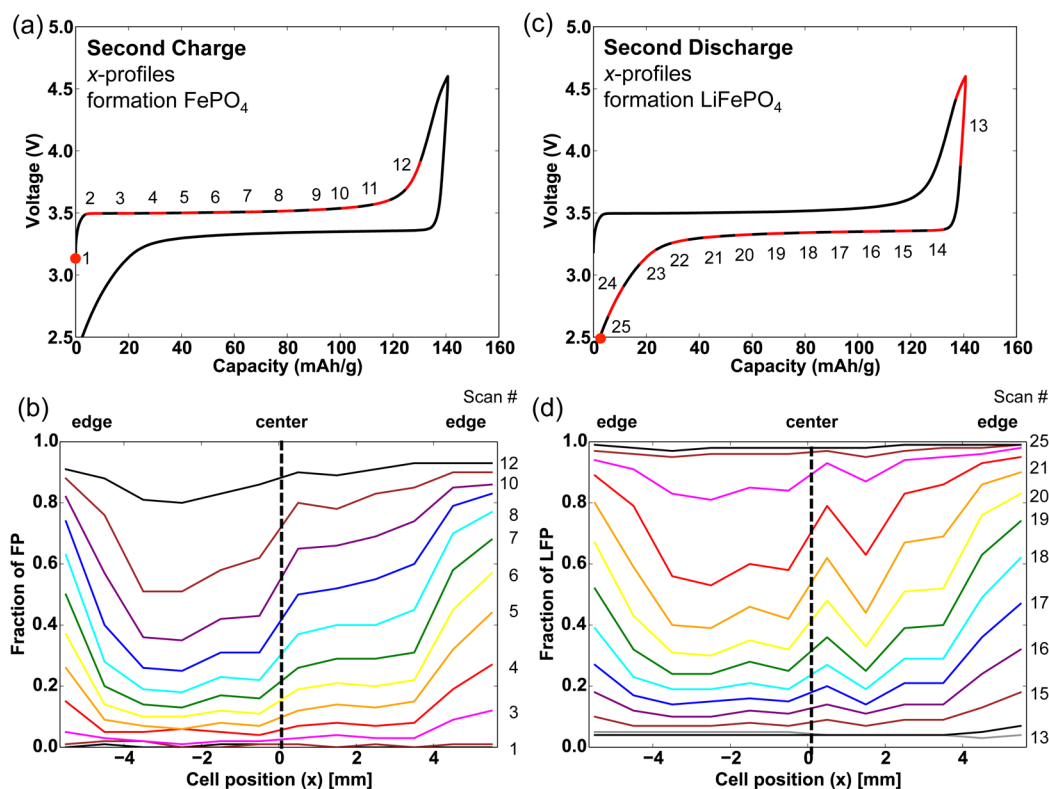


**Figure 10.** *x*-Profiling upon (a,b) charge and (c,d) discharge at a charge rate of  $C/7$  on the second cycle. Parts a and c show the voltage as a function of the capacity. The phase fraction of (b) FP and (d) LFP is plotted as a function of position in the cell, where 0 mm is the center of the electrode. All of the *x*-profiling experiments were carried out at  $y = 150 \mu\text{m}$  (i.e., at the midpoint of the electrode).

the electrode having shorter Li diffusion pathway, but the gradient is less significant than in the *y*-direction. There is an anomaly at 0–2 mm, which is more pronounced on discharge (shown in Figure 10d) and is attributed to a fault in the electrode fabrication. The reaction profile from the EDXRD experiments is asymmetric with respect to the center (at 0 mm, shown by a vertical dotted line in Figure 10b,d). On the basis of the data, the particles on the right-hand side appear to react

faster than the particles on the left-hand side; this is further discussed below.

Figure 11 shows the simulation results for the *x*-profiling of the second cycle. In Figure 11a, when the sample is perfectly aligned, the simulation results are symmetrical since there are no asymmetries in any of the governing equations or in the boundary conditions. The agreement between this result and the experiment is poor as the experimental *x*-profiles show a

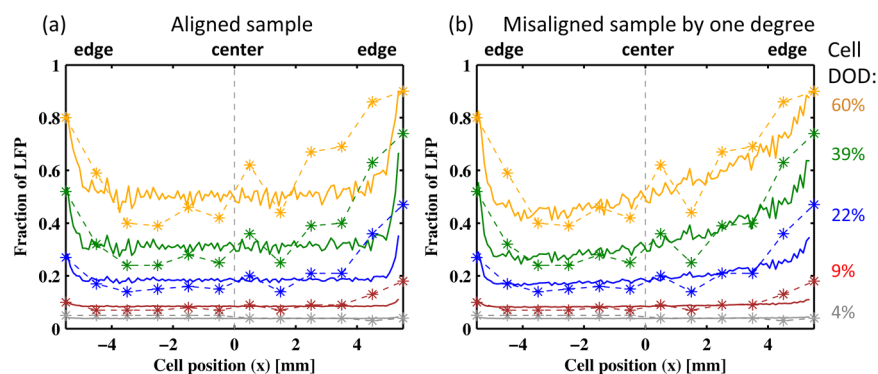


**Figure 11.** Fraction of LFP in the  $x$ -direction for the second discharge simulation (a) with a perfectly aligned beam and (b) with a beam misaligned by  $1^\circ$  in the  $y$ -direction. The solid lines indicate the simulation results, and the dashed lines with markers indicate the experimental results.

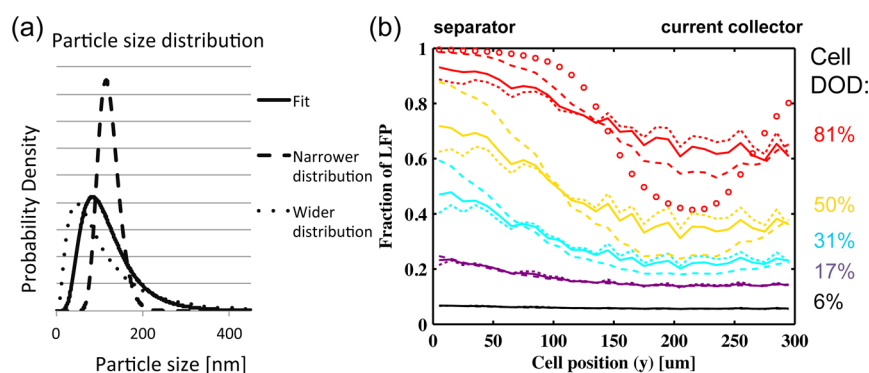


**Figure 12.** (a) Particle-size distribution and (b)  $y$ -profiling for different size distributions. The solid curves indicate the fitted distribution, the dashed curves indicate a narrower distribution, and the dotted curves indicate a wider distribution. The circular markers (provided only for cell DOD = 81%) indicate the case with single-sized particles.

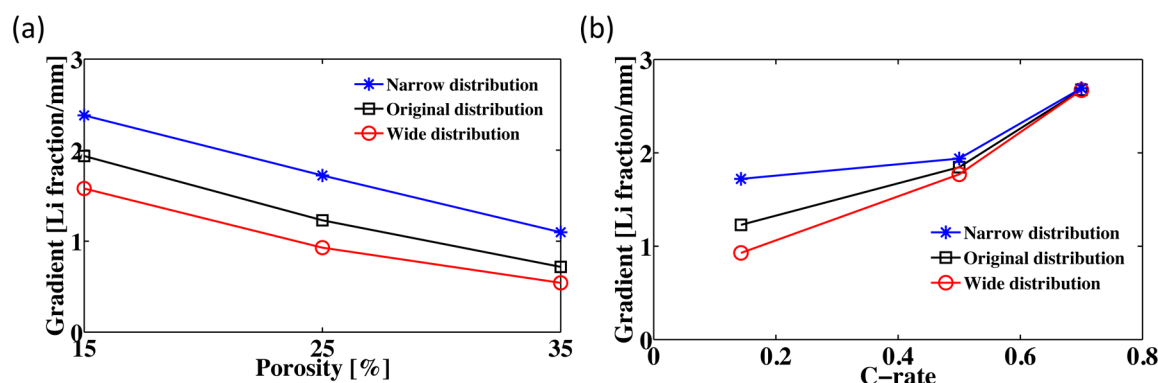
strong asymmetry. While other causes such as a variation in the pressure on the cell are likely, we hypothesize that there was a small (only  $\sim 1^\circ$ ) misalignment of the battery in the coin cell holder on the stage, which is within the uncertainty of the experimental setup. Such a small misalignment would cause the sampled region on the right side of the cell to be  $\sim 200\ \mu\text{m}$  closer to the separator than that on the left side. Figure 11b shows the simulation data assuming this misalignment. Good agreement with the experimental results is now observed, including the asymmetric shape of the concentration profile, which indicates that the asymmetry in the profiles largely originates from the higher fraction of LFP closer to the separator in comparison to the fraction of LFP closer to the current collector. Furthermore, the good agreement of the “cup” appearance of the profiles with the simulations suggests that the pooling of the electrolyte at the edges is a key contribution to the variation in the  $x$ -direction. Hence, the experimental observations are not a result of the higher pressures at the edges than in the middle. Differences between our study and prior work<sup>21</sup> likely originate from the differences in cell design.

Figure S3 in the Supporting Information shows a comparison between the LFP/FP ratios determined electrochemically vs those determined by Rietveld refinement for both  $x$ - and  $y$ -profiling. In all cases, the phase fraction of LFP determined by refinement at the top of charge is only 4–7% in the  $y$ -profiles and 12% in the  $x$ -profiles, while only 81% of theoretical capacity is obtained electrochemically. This strongly suggests that there are parts of the coin cell that were either under lower stack pressure or were not well electrically/ionically wired,

which were not profiled in these experiments. The nonuniform pressure is inherent to the design of a coin cell, given the wave-like spring used in these cells (see the Supporting Information). Furthermore, this suggests that nonuniform pressure on the coin cell might also be playing an additional role in the asymmetry seen on  $x$ -profiling. (Reduced pressure can result in poorer electrical contacts between particles.)

**Simulations for Electrode Design.** Having verified the agreement between the experimental and simulation results, we now employ the simulations to explore further the dependence of the  $y$ -profile gradients on the particle-size distribution, porosity, and C-rate. These analyses are performed to extract information that could be utilized to optimize the electrode architecture and are based on the parameters used for the simulation of the second cycle. To quantify the change in dynamics, we measure the Li-fraction gradient across the cell in the  $y$ -direction. The gradient is measured at a DOD of 50%, at which the differences tend to be significant; it is approximated as (fraction of LFP near separator – fraction of LFP near current collector)/width.

We first analyze the  $y$ -profile for different particle-size distributions. For this analysis, two additional log-normal size distributions with the same average particle size were considered, one wider and the other narrower than that assumed above. The parameters for these two distributions can be found in the Supporting Information. Figure 12a shows the probability density of the different distributions, and Figure 12b shows the resulting  $y$ -profile. We also present the  $y$ -profile for the case in which all the particles are of the same size (circular markers at cell DOD of 81% in Figure 12b). When the



**Figure 13.** Measured  $y$ -profile gradient (at cell DOD = 50%) as a function of (a) porosity and (b) C-rate for the three different particle-size distributions.

distribution is narrower, the position dependence is stronger, which can result in more electrolyte depletion. In contrast, when the distribution is wider, the particles react more homogeneously throughout the cell. Importantly, even though the wider particle-size distribution decreases the net difference in the extent of reaction across the electrode, our earlier work has shown that wider particle-size distributions react more inhomogeneously at shorter length scales.<sup>36</sup> Furthermore, in the case of single-size distribution, the particles react even more inhomogeneously than in the case of a narrow size distribution. The difference in the results illustrates that simple porous electrode models in which only the average of the particle size is employed are not sufficient to model cells in which the size distribution is not negligible.

We next analyze the  $y$ -profile gradient responses to porosity. For this analysis, the ratio of active to inactive material in the original distribution remained constant, and only porosity (the electrolyte volume fraction) was changed. In addition to the original cell, in which the porosity was approximately 25%, we consider 35% and 15% porosities. In Figure 13a, we calculate the average  $y$ -profile gradient for the different porosities and the different size distributions considered above. When the porosity is increased to 35%, the Li-concentration gradient decreases, which can be attributed to a higher effective diffusivity of the ions in the electrolyte. Similarly, when the porosity is decreased to 15%, the Li-concentration gradient increases. Thus, a higher porosity facilitates the homogenization of particle reactions. A similar trend is observed for the different size distributions. However, it is important to note that when the porosity is increased, the fraction of active material is reduced, thereby decreasing the volumetric energy density of the battery.

Finally, we analyze the discharge dynamics at different C-rates. Figure 13b shows the gradients of the  $y$ -profile at C/2 and 0.7C in addition to the original C/7 data for different particle-size distributions. The concentration gradients increase as the rate increases, which reflect the fact that, at higher rates, the Li diffusion in the electrolyte becomes more limiting. Interestingly, as the C-rate increases, the dependence of the  $y$ -profile gradients on the particle-size distribution decreases and the three different size distributions tend to converge to a similar gradient.

## CONCLUSIONS

We have performed experiments and simulations to examine the inhomogeneity of the electrochemical reaction of an LFP-electrode in a standard coin cell battery. In the first cycle, the

reaction occurs preferentially in LFP particles in the electrode that are closer to the separator and thus the source of  $\text{Li}^+$  ions, indicating that the kinetics of Li-diffusion in the electrolyte, within the pores of the electrode, dominates. However, on the second cycle, we observed a change in the reaction profile through the electrode. Now two Li phase-fraction gradients are seen, each dominated by a different rate-limiting mechanism. The half of the electrode closer to the current collector exhibited preferential delithiation compared with the middle of the electrode, which suggests electronic limitations, while the higher delithiation next to the separator is again ascribed to the high tortuosity of Li ionic transport in and out of the thick electrode. The 3D simulations are in good agreement with the experimental results for both the first and second cycles. The simulations suggest that the electronic conductivity of the electrode is eight times smaller for the second cycle than for the first cycle. The reduced electronic conductivity may be caused by the particle expansion and contraction upon cycling, resulting in poorer particle–particle contacts, leading to poorer electronic wiring. The role that SEI formation on the cathode plays cannot be ignored<sup>53,54</sup> and will be explored in future studies. However, the gradient arising from limitation in electronic conductivity was less significant than the gradient due to limitation of Li-ion diffusion in the electrolyte. When profiling in the  $x$ -direction, perpendicular to the applied current, preferential reactivity was observed in the particles that were closer to the sides of the cathode than in the center. The preferential reactivity suggests Li diffusion-limited kinetics in the  $x$ -direction, presumably due to pooling of electrolyte around the edges of the electrode film. However, the preferential reactivity was less significant than the  $y$ -direction gradient, which is parallel to the applied current.

The theoretical model employed in this study was then used to explore the reaction inhomogeneity as a function of the current, porosity, and particle-size distribution. Increasing the porosity improves the reaction homogeneity throughout the cathode; however, it decreases the volumetric energy density of the electrode. When particle-size distribution is widened, the electrochemical reaction becomes more evenly distributed over the length scale of the cell because the dependence of the particles on their position in the electrode diminishes. However, it causes the particles to react more inhomogeneously locally (smaller particles reacting in preference to nearby larger particles). The effect of a different size distribution on the reaction gradient across the electrode was only a significant



phenomenon for C-rates smaller than C/2, after which the gradient converged to similar values that increase with the rate.

To conclude, our combined experimental and theoretical study has demonstrated the importance of effective Li-ion transport and electronic wiring in LFP-electrodes to achieve a homogeneous reaction at the whole-electrode level. The combination of theory and experiment was critical because it allowed the relative importance of the various rate-limiting phenomena to be evaluated. Additionally, we have considered the significance of the particle-size distribution, the porosity of the electrode, and the cycle rate to the inhomogeneity of the electrochemical reaction. The practical consequences of inhomogeneity can be severe, particularly for large (and high power) batteries, since it can result in large distributions of potential across the electrode. This can either result in capacity loss since parts of the positive and negative electrodes do not achieve the required potential for lithiation/delithiation and/or can result in overcharge in other parts of the electrode. Overcharging can result in more rapid electrolyte break down and can have safety implications.

Finally, we believe that the combination of EDXRD and microfocused diffraction is a novel technique to study the progression of reaction fronts (and the kinetics of reaction) through composite structures in a wide range of materials systems beyond the battery chemistry studied here. Potential applications include studies of carbonation reactions (of relevance to carbon capture chemistry), gas sorption in fluidized beds, and phase changes in general, where the stimulus for the change (temperature, pressure, etc.) is nonuniform or varies in time.

## ■ ASSOCIATED CONTENT

### ■ Supporting Information

Additional information on the EDXRD experiments carried out at the National Synchrotron Light Source at Brookhaven National Laboratory using polyvinylidene fluoride as the binder in the electrode; EDXRD patterns and refinements of the data at the start of the first and second charge; the comparison between the DOD of the bulk electrochemistry and the average profiles from the EDXRD experiments; the details of the model and simulations; X-ray diffraction pattern of the as-synthesized  $\text{LiFePO}_4$  and refinement using the Topas software; scanning electron microscope images of the  $\text{LiFePO}_4$  particles and the particle-size distribution of  $\text{LiFePO}_4$  particles in the electrode; the EDXRD data from the first charge plotted with error bars; the tabulated data of the DOD calculated from the electrochemistry, the EDXRD experiments and the simulations and a picture of the spring used in this study. This material is available free of charge via the Internet at <http://pubs.acs.org>.

## ■ AUTHOR INFORMATION

### Corresponding Author

\*E-mail: [cpg27@cam.ac.uk](mailto:cpg27@cam.ac.uk)

### Present Address

#R.R.: Paul Scherrer Institut, Electrochemistry Laboratory, CH-5232 Villigen PSI, Switzerland

### Author Contributions

○F.C.S. and B.O. contributed equally.

The manuscript was written with contributions from all the authors.

### Notes

The authors declare no competing financial interest.

## ■ ACKNOWLEDGMENTS

We acknowledge the Engineering Physical Science Research Council (EPSRC) for a Doctoral Training Account Award (for FCS) and the US Department of Energy (DOE) for support via the NECCES, an Energy Frontier Research Center (DE-SC0001294 and DE-SC0012583). FCS acknowledges the Science and Technology Facilities Council for travel funding through the Global Challenge Network in Batteries and Electrochemical Energy Devices. Synchrotron X-ray beamtime was provided by Diamond Light Source, under experiment number EE8385. We also thank Zlatko Saracevic at the Department of Chemical Engineering at the University of Cambridge for help with the BET experiments and Jon Rickard at the Department of Physics at the University of Cambridge for help with the SEM. Lastly, we thank Charles Monroe and Paul Shearing for discussions on this project.

## ■ ABBREVIATIONS

LFP,  $\text{LiFePO}_4$ ; FP,  $\text{FePO}_4$ ; C-LFP, carbon-coated  $\text{LiFePO}_4$ ; 1D, one-dimensional; 3D, three-dimensional; XRD, X-ray diffraction; EDXRD, energy-dispersive X-ray diffraction; PTFE, polytetrafluorethylene; PVDF, polyvinylidene fluoride; CNF, carbon nanofibers; SEM, scanning electron microscopy; BET, Brunauer–Emmett–Teller; BJH, Barrett–Joyner–Halenda; DOD, depth of discharge

## ■ REFERENCES

- (1) Padhi, A. K.; Nanjundaswamy, K. S.; Goodenough, J. B. *J. Electrochem. Soc.* **1997**, *144*, 1188–1194.
- (2) Andersson, A. S.; Thomas, J. O.; Kalska, B.; Haggstrom, L. *Electrochem. Solid-State Lett.* **2000**, *3*, 66–68.
- (3) Chung, S.-Y.; Bloking, J. T.; Chiang, Y.-M. *Nat. Mater.* **2002**, *1*, 123–128.
- (4) Chen, J.; Graetz, J. *ACS Appl. Mater. Interfaces* **2011**, *3*, 1380–1384.
- (5) Yonemura, M.; Yamada, A.; Takei, Y.; Sonoyama, N.; Kanno, R. *J. Electrochem. Soc.* **2004**, *151*, A1352.
- (6) Malik, R.; Burch, D.; Bazant, M.; Ceder, G. *Nano Lett.* **2010**, *10*, 4123–4127.
- (7) Mizushima, K.; Jones, P. C.; Wiseman, P. J.; Goodenough, J. B. *Mater. Res. Bull.* **1980**, *15*, 783–789.
- (8) Huang, H.; Yin, S. C.; Nazar, L. F. *Electrochem. Solid-State Lett.* **2001**, *4*, A170.
- (9) Kang, B.; Ceder, G. *Nature* **2009**, *457*, 190–193.
- (10) Wang, Q.; Zhang, W.; Yang, Z.; Weng, S.; Jin, Z. *J. Power Sources* **2011**, *196*, 10176–10182.
- (11) Pei, B.; Wang, Q.; Zhang, W.; Yang, Z.; Chen, M. *Electrochim. Acta* **2011**, *56*, S667–S672.
- (12) Omenya, F.; Chernova, N. A.; Zhang, R.; Fang, J.; Huang, Y.; Cohen, F.; Dobrzynski, N.; Senanayake, S.; Xu, W.; Whittingham, M. S. *Chem. Mater.* **2013**, *25*, 85–89.
- (13) Meethong, N.; Kao, Y.-H.; Speakman, S. A.; Chiang, Y.-M. *Adv. Funct. Mater.* **2009**, *19*, 1060–1070.
- (14) Burch, D. *Intercalation Dynamics in Li-ion Batteries*. Ph.D Thesis, Massachusetts Institute of Technology, Cambridge, MA, 2009.
- (15) Delmas, C.; Maccario, M.; Croguennec, L.; Le Cras, F.; Weill, F. *Nat. Mater.* **2008**, *7*, 665–671.
- (16) Malik, R.; Zhou, F.; Ceder, G. *Nat. Mater.* **2011**, *10*, 587–590.
- (17) Liu, H.; Strobridge, F. C.; Borkiewicz, O. J.; Wiaderek, K. M.; Chapman, K. W.; Chupas, P. J.; Grey, C. P. *Science* **2014**, *344*, 1252817–1252817.
- (18) Zhang, X.; van Hulzen, M.; Singh, D. P.; Brownrigg, A.; Wright, J. P.; van Dijk, N. H.; Wagemaker, M. *Nano Lett.* **2014**, *14*, 2279–2285.
- (19) Liu, J.; Kunz, M.; Chen, K.; Tamura, N.; Richardson, T. J. *J. Phys. Chem. Lett.* **2010**, *1*, 2120–2123.

- (20) Robert, D.; Douillard, T.; Boulineau, A.; Brunetti, G.; Nowakowski, P.; Venet, D.; Bayle-Guillemaud, P.; Cayron, C. *ACS Nano* **2013**, *7*, 10887–10894.
- (21) Ouvrard, G.; Zerrouki, M.; Soudan, P.; Lestriez, B.; Masquelier, C.; Morcrette, M.; Hamelet, S.; Belin, S.; Flank, A. M.; Baudalet, F. *J. Power Sources* **2013**, *229*, 16–21.
- (22) Leriche, J. B.; Hamelet, S.; Shu, J.; Morcrette, M.; Masquelier, C.; Ouvrard, G.; Zerrouki, M.; Soudan, P.; Belin, S.; Elkaim, E.; Baudalet, F. *J. Electrochem. Soc.* **2010**, *157*, A606.
- (23) Johns, P. A.; Roberts, M. R.; Wakizaka, Y.; Sanders, J. H.; Owen, J. R. *Electrochem. Commun.* **2009**, *11*, 2089–2092.
- (24) Roberts, M. R.; Madsen, A.; Nicklin, C.; Rawle, J.; Palmer, M. G.; Owen, J. R.; Hector, A. L. *J. Phys. Chem. C* **2014**, *118*, 6548–6557.
- (25) Orvananos, B.; Ferguson, T. R.; Yu, H.-C.; Bazant, M. Z.; Thornton, K. *J. Electrochem. Soc.* **2014**, *161*, A535–A546.
- (26) Van der Ven, A.; Wagemaker, M. *Electrochem. Commun.* **2009**, *11*, 881–884.
- (27) Cogswell, D. A.; Bazant, M. Z. *Nano Lett.* **2013**, *13*, 3036–3041.
- (28) Orvananos, B.; Malik, R.; Yu, H.-C.; Abdellahi, A.; Grey, C. P.; Ceder, G.; Thornton, K. *Electrochim. Acta* **2014**, *137*, 245–257.
- (29) Bae, C.-J.; Erdonmez, C. K.; Halloran, J. W.; Chiang, Y.-M. *Adv. Mater.* **2012**, *25*, 1254–1258.
- (30) Fongy, C.; Jouanneau, S.; Guyomard, D.; Lestriez, B. *J. Power Sources* **2011**, *196*, 8494–8499.
- (31) Ebner, M.; Chung, D.-W.; García, R. E.; Wood, V. *Adv. Energy Mater.* **2013**, *4*, 1301278.
- (32) Croft, M.; Zhong, Z.; Jisrawi, N.; Zakharchenko, I.; Holtz, R.; Skaritka, J.; Fast, T.; Sadananda, K.; Lakshminpathy, M.; Tsakalakos, T. *Int. J. Fatigue* **2005**, *27*, 1408–1419.
- (33) Croft, M.; Jisrawi, N.; Zhong, Z.; Horvath, K.; Holtz, R. L.; Shepard, M.; Lakshminpathy, M.; Sadananda, K.; Skaritka, J.; Shukla, V.; Sadangi, R. K.; Tsakalakos, T. *J. Eng. Mater. Technol.* **2008**, *130*, 021005.
- (34) Croft, M.; Shukla, V.; Akdoğan, E. K.; Jisrawi, N.; Zhong, Z.; Sadangi, R.; Ignatov, A.; Balarinni, L.; Horvath, K.; Tsakalakos, T. *J. Appl. Phys.* **2009**, *105*, 093505.
- (35) Liang, G.; Croft, M. C.; Zhong, Z. *J. Electrochem. Soc.* **2013**, *160*, A1299–A1303.
- (36) Liu, Q.; He, H.; Li, Z.-F.; Liu, Y.; Ren, Y.; Lu, W.; Lu, J.; Stach, E. A.; Xie, J. *ACS Appl. Mater. Interfaces* **2014**, *6*, 3282–3289.
- (37) Takeuchi, E. S.; Marschilok, A. C.; Takeuchi, K. J.; Ignatov, A.; Zhong, Z.; Croft, M. *Energy Environ. Sci.* **2013**, *6*, 1465.
- (38) Kirshenbaum, K.; Bock, D. C.; Lee, C.-Y.; Zhong, Z.; Takeuchi, K. J.; Marschilok, A. C.; Takeuchi, E. S. *Science* **2015**, *347*, 145–149.
- (39) Kobayashi, G.; Nishimura, S.-I.; Park, M.-S.; Kanno, R.; Yashima, M.; Ida, T.; Yamada, A. *Adv. Funct. Mater.* **2009**, *19*, 395–403.
- (40) Coelho, A. A. *Acta Crystallogr.* **2007**, *63*, 400–406.
- (41) Scarlett, N. V. Y.; Madsen, I. C.; Evans, J. S. O.; Coelho, A. A.; McGregor, K.; Rowles, M.; Lanyon, M. R.; Urban, A. J. *J. Appl. Crystallogr.* **2009**, *42*, 502–512.
- (42) Chueh, W. C.; El Gabaly, F.; Sugar, J. D.; Bartelt, N. C.; McDaniel, A. H.; Fenton, K. R.; Zavadil, K. R.; Tyliszczak, T.; Lai, W.; McCarty, K. F. *Nano Lett.* **2013**, *13*, 866–872.
- (43) Ferguson, T. R.; Bazant, M. Z. *J. Electrochem. Soc.* **2012**, *159*, A1967–A1985.
- (44) Newman, J.; Tiedeman, W. *AIChE J.* **1975**, *21*, 25–41.
- (45) Li, Y.; El Gabaly, F.; Ferguson, T. R.; Smith, R. B.; Bartelt, N. C.; Sugar, J. D.; Fenton, K. R.; Cogswell, D. A.; Kilcoyne, A. L. D.; Tyliszczak, T.; Bazant, M. Z.; Chueh, W. C. *Nat. Mater.* **2014**, *13*, 1149–1156.
- (46) Darling, R.; Newman, J. *J. Electrochem. Soc.* **1997**, *144*, 4201–4208.
- (47) Kang, H.-C.; Jun, D.-K.; Jin, B.; Jin, E. M.; Park, K.-H.; Gu, H.-B.; Kim, K.-W. *J. Power Sources* **2008**, *179*, 340–346.
- (48) Yang, X.; Liu, D.; Xu, X.; He, X.; Xie, J. *CrystEngComm* **2013**, *15*, 10648.
- (49) Hamelet, S.; Gibot, P.; Casas-Cabanas, M.; Bonnin, D.; Grey, C. P.; Cabana, J.; Leriche, J.-B.; Rodriguez-Carvajal, J.; Courty, M.; Levasseur, S.; Carlach, P.; Van Thournout, M.; Tarascon, J.-M.; Masquelier, C. *J. Mater. Chem.* **2009**, *19*, 3979.
- (50) Zhang, L.; Xiang, H.; Zhu, X.; Yang, W.; Wang, H. *J. Mater. Sci.* **2011**, *47*, 3076–3081.
- (51) Kameda, Y.; Umebayashi, Y.; Takeuchi, M.; Wahab, M. A.; Fukuda, S.; Ishiguro, S.-I.; Sasaki, M.; Amo, Y.; Usuki, T. *J. Phys. Chem. B* **2007**, *111*, 6104–6109.
- (52) Newman, J. S.; Tobias, C. W. *J. Electrochem. Soc.* **2006**, *109*, 1183–1191.
- (53) Malmgren, S.; Rensmo, H.; Gustafsson, T.; Gorgoi, M.; Edström, K. *ECS Trans.* **2010**, *25*, 201–210.
- (54) Zhong, K.; Cui, Y.; Xia, X.-D.; Xue, J.-J.; Liu, P.; Tong, Y.-X. *J. Power Sources* **2014**, *250*, 296–305.